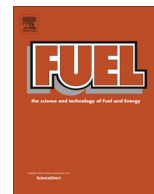




Contents lists available at ScienceDirect

Fuel

journal homepage: [www.elsevier.com/locate/fuel](http://www.elsevier.com/locate/fuel)



# Influences of cation and anion substitutions on oxidative coupling of methane over hydroxyapatite catalysts

Su Cheun Oh<sup>a</sup>, Yiqing Wu<sup>a</sup>, Dat T. Tran<sup>b</sup>, Ivan C. Lee<sup>b</sup>, Yu Lei<sup>c</sup>, Dongxia Liu<sup>a,\*</sup>

<sup>a</sup> Department of Chemical and Biomolecular Engineering, University of Maryland, College Park, MD 20742, USA

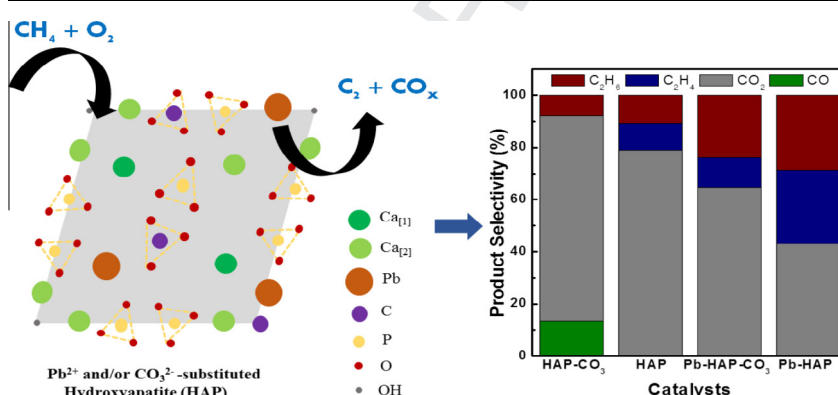
<sup>b</sup> U.S. Army Research Laboratory, RDRL-SED-E, 2800 Powder Mill Road, Adelphi, MD 20783, USA

<sup>c</sup> Chemical and Materials Engineering, The University of Alabama in Huntsville, 301 Sparkman Drive, Huntsville, AL 35899, USA

## HIGHLIGHTS

- $\text{Pb}^{2+}$ ,  $\text{CO}_3^{2-}$  and both substitutions in hydroxyapatite (HAP) were studied.
- Structural properties and performance of HAP catalysts in OCM reactions were revealed.
- $\text{Pb-HAP-CO}_3$  exhibits the best stability and  $\text{C}_2$  yield under optimized conditions.
- Tuning compositions of HAP by ion substitutions tailors its OCM performances.

## GRAPHICAL ABSTRACT



## ARTICLE INFO

### Article history:

Received 6 August 2015  
Received in revised form 15 November 2015  
Accepted 16 November 2015  
Available online xxxx

### Keywords:

Hydroxyapatite  
Membrane reactor  
Anion and cation substitution  
Methane  
Oxidative coupling

## ABSTRACT

Lead substituted hydroxyapatite (Pb-HAP) has been an active catalyst for oxidative coupling of methane (OCM) reactions.  $\text{CO}_3^{2-}$  substituted HAP (HAP- $\text{CO}_3$ ) has showed enhanced oxide ion conductivity than bare HAP in high temperature solid oxide fuel cells. Substitutions for both cations and anions in HAP structure (Pb-HAP- $\text{CO}_3$ ) are promising to integrate the catalytic property of Pb-HAP and oxide ion conductive property of HAP- $\text{CO}_3$  into one apatite-based ceramic material that can be manufactured into membrane reactors for possessing  $\text{CH}_4$  activation and  $\text{O}_2$  permeation capabilities for efficient OCM reactions. In this work, the effects of substitutions for both cation ( $\text{Pb}^{2+}$ ) and anion ( $\text{CO}_3^{2-}$ ) in HAP structure on OCM reactions were studied. The composition and physicochemical properties of HAP catalysts were changed by the cation and anion substitutions, respectively, and as consequences, they influenced the catalytic performances of HAP structure in OCM reactions. The selectivity to  $\text{C}_2$  (ethylene and ethane) products increased in the order of  $\text{HAP-CO}_3 < \text{HAP} < \text{Pb-HAP-CO}_3 < \text{Pb-HAP}$ , while Pb-HAP- $\text{CO}_3$  showed the best stability and comparable  $\text{C}_2$  yield (under optimized reaction conditions) to Pb-HAP catalyst. Under different reaction temperature and/or  $\text{CH}_4/\text{O}_2$  ratio in the OCM reactions, the  $\text{CH}_4$  conversion and  $\text{C}_2$  or  $\text{CO}_x$  (CO and  $\text{CO}_2$ ) selectivity showed a strong dependence on the composition of HAP-based catalysts. The present study forms a basis for understanding of the correlations between the composition, structure, and catalytic performance of HAP and other apatite structured catalysts, which are potential membrane materials for OCM reactions in membrane reactors.

© 2015 Published by Elsevier Ltd.

\* Corresponding author. Tel.: +1 301 405 3522; fax: +1 301 405 0523.

E-mail address: [liud@umd.edu](mailto:liud@umd.edu) (D. Liu).

## 1. Introduction

The depletion of crude oil is shifting the market attention to natural gas that is still of great abundance [1,2]. Natural gas is made up of mainly methane ( $\text{CH}_4$ ), which can substitute liquid petroleum for power generation and be a raw material in petrochemical industries. Rigorous research efforts have been made to convert methane into liquid fuels or chemicals. The most widely studied methane conversion processes include dry and steam reforming of methane to synthesis gas ( $\text{CO} + \text{O}_2$ ) followed by Fischer–Tropsch synthesis of higher hydrocarbons [3], non-oxidative direct methane conversion to aromatics [4,5], and direct oxidative coupling of methane (OCM) to  $\text{C}_2$  hydrocarbon [6,7]. In comparison with the first two processes, OCM is potentially more selective and economical given its unique capability in forming  $\text{C}_2$  ( $\text{C}_2\text{H}_4$  and  $\text{C}_2\text{H}_6$ ) hydrocarbons while circumventing the intermediate energy intensive steps in synthesis gas approach and fast catalyst deactivation by coke deposition in methane-to-aromatics approach. The more reactive nature of  $\text{C}_2$  products than methane in OCM reactions, however, leads to the sequential oxidation of  $\text{C}_2$  to  $\text{CO}_x$  ( $\text{CO}$  or  $\text{CO}_2$ ). The attainable  $\text{C}_2$  yield in the OCM process is limited to 28% under a fixed-bed, continuous-feed reaction condition [8].

Membrane reactors comprised of active catalysts and  $\text{O}_2$  permeable membranes have potential to mitigate the limit on  $\text{C}_2$  yield in the OCM process [9]. The OCM reaction by catalytic membrane reactors involves both surface and gas-phase reactions. The  $\text{O}_2$  permeable membranes serve as  $\text{O}_2$  distributors to regulate gaseous  $\text{O}_2$  concentration in the reactor, which restricts the consecutive oxidation of  $\text{C}_2$  to  $\text{CO}_x$ . Although a substantial enhancement of the  $\text{C}_2$  yield has been predicted when an  $\text{O}_2$  permeable membrane was used in conjunction with an active OCM catalyst [10,11], the parallel experimental studies on the OCM process in membrane reactors were not favorable due to lack of membranes with sufficient and harmonized catalytic and  $\text{O}_2$  permeable properties, and lack of rigorous description of the  $\text{O}_2$  kinetic effects on the OCM process in membrane reactors.

Hydroxyapatite ( $\text{Ca}_{10}(\text{PO}_4)_6(\text{OH})_2$ ) is a type of calcium phosphate crystal more commonly studied in biomaterials because it is a major constituent of teeth and bones [12]. HAP has a hexagonal structure which is stable up to 1273 K, and is comprised of 10  $\text{Ca}^{2+}$  ions located on two sets of non-equivalent sites, 4  $\text{Ca}_{[1]}$  on site 1 and 6  $\text{Ca}_{[2]}$  on site 2 in one unit cell [13]. The  $\text{Ca}_{[1]}$  is coordinated to 6 oxygen atoms belonging to different  $\text{PO}_4$  tetrahedra and also to 3 oxygen atoms at a larger distance. The  $\text{Ca}_{[2]}$  is found in cavities in the walls of the channels formed between the Ca and O atoms [14]. The  $\text{Ca}^{2+}$  cation and the anion, either  $\text{PO}_4^{3-}$  in the B-site or  $\text{OH}^-$  in the A-site, can be substituted by other cation or anions using co-precipitation of a mixed cation and anion precursor solutions [15–17], sorption of cation solution onto HAP structure [18] as well as simple mixing of calcium hydroxide with a cation containing orthophosphoric acid solution [19]. These synthesis methods endow HAP with tunable thermal and chemical stability [20], catalytic properties [21,22], and ion/electronic conductive properties [23]. Pb can substitute either  $\text{Ca}_{[1]}$  or  $\text{Ca}_{[2]}$ , or both depending on the Pb concentrations in the structure, and Pb-HAP were able to increase  $\text{C}_2$  selectivity by a factor of 5 compared to bare HAP [24]. Recent report on B-site substituted HAP- $\text{CO}_3$ , in which the  $\text{PO}_4^{3-}$  of HAP was partially substituted by  $\text{CO}_3^{2-}$ , showed that the oxide ion conduction was comparable to the yttria-stabilized-zirconia superionic conductor at 973 K [25]. Given the catalytic property of Pb-HAP and oxide ion conductive property of HAP- $\text{CO}_3$ , Pb-HAP- $\text{CO}_3$  is a promising apatite-based ceramic membrane material possessing  $\text{CH}_4$  activation and  $\text{O}_2$  permeation capabilities for efficient OCM reactions. Systematic investigation on both cation and anion substituted HAP in OCM reactions, however, is rarely accessible.

In the present work, we report the synthesis of HAP catalysts with cation (Pb-HAP), anion (HAP- $\text{CO}_3$ ), and both cation and anion (Pb-HAP- $\text{CO}_3$ ) substitutions. The effects of substitutions on physicochemical and acidity/basicity properties, and catalytic behaviors of HAP-based catalysts were assessed. X-ray diffraction (XRD), scanning electron microscopy (SEM), nitrogen adsorption, Fourier transform infrared (FTIR) and Raman spectroscopy, temperature programmed desorption of ammonia ( $\text{NH}_3$ -TPD), X-ray photoelectron spectroscopy (XPS) and X-ray absorption fine structure spectroscopy (XAFS) were used to characterize the structural and physicochemical properties of the HAP-based catalysts. The catalytic behaviors of the HAP-based catalysts in OCM reactions were examined. It is shown that cation or anion substitution can change the composition and physicochemical properties of the HAP-based catalysts, and as consequences, the catalytic behaviors of HAP-based materials in OCM reactions.

## 2. Experimental

### 2.1. Materials

Ammonium phosphate dibasic ( $(\text{NH}_4)_2\text{HPO}_4$ ,  $\geq 99.0\%$ ), ammonium chloride ( $\text{NH}_4\text{Cl}$ ,  $\geq 99.5\%$ ) and ammonia hydroxide solution ( $\text{NH}_4\text{OH}$ , 28–30%) were supplied from Sigma–Aldrich. Lead nitrate ( $\text{Pb}(\text{NO}_3)_2$ , A.C.S. Reagent) was purchased from J.T. Baker. Sodium bicarbonate ( $\text{NaHCO}_3$ , 99.7–100.3%) was provided by BDH. Calcium nitrate tetrahydrate ( $\text{Ca}(\text{NO}_3)_2 \cdot 4\text{H}_2\text{O}$ ,  $>99.5$  purity) was purchased from Alfa-Aesar.

### 2.2. HAP-based catalysts preparation

The synthesis of bare HAP was carried out by first preparing a solution of  $(\text{NH}_4)_2\text{HPO}_4$  (0.25 M, 480 mL) in one flask and a solution of  $\text{Ca}(\text{NO}_3)_2$  (0.37 M, 320 mL) in a second flask. After pH of each solution was raised to  $\sim 10$  with  $\text{NH}_4\text{OH}$ , the two source solutions were mixed together by adding  $(\text{NH}_4)_2\text{HPO}_4$  solution via a syringe pump ( $4 \text{ mL min}^{-1}$ ) to  $\text{Ca}(\text{NO}_3)_2$  solution that was preheated to 363 K in an oil bath and was equipped with a reflux condenser. After addition of the  $(\text{NH}_4)_2\text{HPO}_4$  solution, a milky white suspension was obtained and the suspension was kept at 363 K under magnetic stirring overnight followed by aging for 24 h at room temperature. Finally, the product was collected by centrifugation at 6000 rpm for 5 min and washed by dispersing in deionized (DI) water. The water washing and centrifugation steps were repeated 5 times. A vacuum oven was utilized to dry the wet product at 343 K overnight.

In the synthesis of HAP- $\text{CO}_3$  catalyst, the same procedure as that for HAP was employed except that a solution consisting of  $(\text{NH}_4)_2\text{HPO}_4$  (0.25 M) and  $\text{NaHCO}_3$  (0.17 M) was prepared to replace 0.25 M  $(\text{NH}_4)_2\text{HPO}_4$  solution in HAP synthesis. For synthesis of Pb-HAP- $\text{CO}_3$  catalyst, the  $\text{Ca}(\text{NO}_3)_2$  solution in the second flask was replaced with a solution of  $\text{Ca}(\text{NO}_3)_2$  (0.4 M) and  $\text{Pb}(\text{NO}_3)_2$  (0.1 M). The rest of procedure was the same as that for synthesis of HAP- $\text{CO}_3$  catalyst. The synthesis of Pb-HAP catalyst followed a reported procedure [16], which was similar to synthesis of bare HAP above except that an aqueous solution of  $\text{Pb}(\text{NO}_3)_2$  (0.1 M),  $\text{Ca}(\text{NO}_3)_2$  (0.4 M) and  $\text{NH}_4\text{Cl}$  (1.3 M) was prepared to replace  $\text{Ca}(\text{NO}_3)_2$  (0.25 M) in HAP synthesis.

Finally, the vacuum dried HAP-based samples were calcined in flowing air ( $150 \text{ mL min}^{-1}$ , ultrapure, Airgas) at 823 K for 5 h at a ramp rate of  $17.5 \text{ K min}^{-1}$  from ambient temperature. All the samples were pelleted, crushed, and sieved to retain particle sizes between 180 and  $425 \mu\text{m}$  (40–80 mesh) for the following characterization and catalysis experiments.

### 2.3. Catalysts characterization

The morphologies of the HAP-based catalysts were observed by scanning electron microscopy (SEM) on a Hitachi SU-70 electron microscope. The crystallinity of the catalysts were examined by powder X-ray diffraction (XRD) patterns using a Bruker D8 Advance Lynx Powder Diffractometer (LynxEye PSD detector, sealed tube, Cu K $\alpha$  radiation with Ni  $\beta$ -filter). N<sub>2</sub> adsorption-desorption isotherms of the samples were measured using an Autosorb-iQ analyzer (Quantachrome Instruments) at 77 K. The specific surface areas of the samples were determined using (Brunauer, Emmett and Teller) (BET) method. Thermogravimetric analysis (TGA) of the catalyst samples was performed in a TGA instrument (2950, TA Instruments, Inc.) under a mixed air and N<sub>2</sub> flow of 100 mL min<sup>-1</sup> (40% air, 60% N<sub>2</sub>) with a heating rate of 10 K min<sup>-1</sup> from 308 K to 1273 K. Elemental composition of the catalysts was determined by inductively coupled plasma optical emission spectroscopy (ICP-EOS, Optima 4300DV Instrument, Perkin-Elmer). The FTIR spectra of the samples were recorded with a spectrometer (Nicolet Magna-IR 560) in the range of 400–4000 cm<sup>-1</sup>. The Raman spectra of the catalysts were collected with a Raman spectrometer (LabRAM Aramis, Horiba Scientific) in the range of 200–2000 cm<sup>-1</sup>. XPS data was measured over a Kratos AXIS 165 spectrometer equipped with 165 mm radius hemispherical analyzer and eight channels/tron detection system coupled with monochromatic Al radiation. The X-ray absorption fine structure spectroscopy (XAFS) measurements at the Pb L<sub>3</sub> edge (~13.036 keV) were conducted on the bending-magnet beamline of the Materials Research Collaborative Access Team (MRCAT) at the Advanced Photon source in Argonne National Laboratory. XAFS data were collected in the transmission mode under ambient condition. PbO, PbO<sub>2</sub> and Pb foil were considered as references and measured at the beamline. The Pb species fraction was calculated by conducting Pb X-ray absorption near edge spectroscopy (XANES) linear combination fittings using Athena in the IFEFFIT software package.

### 2.4. Determination of acidity of catalysts

The surface acidity of the HAP-based catalysts was evaluated by NH<sub>3</sub>-TPD using an Autosorb-iQ instrument (Quantachrome, ASIQM0000-4) equipped with a thermal conductivity detector (TCD). In the measurement, 0.1 g catalyst sample was loaded into a quartz reactor and heated at a rate of 10 K min<sup>-1</sup> to 973 K under He (40 mL min<sup>-1</sup>) and maintained at this temperature for 2 h in order to remove the surface impurities. After being cooled to room temperature under He stream, the catalyst sample was exposed to NH<sub>3</sub> (30 mL min<sup>-1</sup>, ultrapure, Airgas) stream for 0.5 h. Physisorbed NH<sub>3</sub> was then removed by flowing He gas (30 mL min<sup>-1</sup>) for 2 h. Afterward, the catalyst sample was ramped to 1100 K at a ramp rate of 10 K min<sup>-1</sup>, and the NH<sub>3</sub>-TPD profile was recorded during this step.

### 2.5. OCM catalytic test

The catalytic reaction was performed in the reactor system that has been described in our previous work [26]. Typically, 0.3 g of catalyst sample was loaded in a U-shape tubular quartz reactor (10 mm inner diameter) which was placed inside a temperature controlled furnace (National Electric Furnace FA120 type). The temperature of the furnace was controlled by a Watlow Controller (96 series). A K-type thermocouple was attached to the outer wall of the reactor to monitor the temperature of the catalyst environment. The sample was pretreated in He and O<sub>2</sub> atmosphere (33 mL min<sup>-1</sup>, volume ratio: 91% He, 9% O<sub>2</sub>) at 823 K for 4 h prior to the OCM reactions. Afterward, the catalyst was heated to the

desired reaction temperature. The CH<sub>4</sub> (8 mL min<sup>-1</sup>, 99.999% purity, Airgas) and O<sub>2</sub> (3 mL min<sup>-1</sup>, 99.9993% purity, Airgas) diluted in N<sub>2</sub> (5 mL min<sup>-1</sup>, 99.95% purity, Airgas) and He (30 mL min<sup>-1</sup>, 99.9993% purity, Airgas) were sent via heated transfer lines hold at 343 K to the reactor. The reactant and product gases were analyzed using gas chromatograph (Agilent Technologies, 6890N) equipped with ShinCarbon ST packed column connected to a TCD. Dependency of CH<sub>4</sub>/O<sub>2</sub> ratios was studied by changing the flow rates of O<sub>2</sub> and the balance He gases while keeping constant flow rate in CH<sub>4</sub>. The blank test in the reactor without catalysts showed that the methane conversion was less than 1%, suggesting that the gas phase reaction between CH<sub>4</sub> and O<sub>2</sub> was not favored under studied conditions.

## 3. Results and discussion

### 3.1. Textural and structural properties of catalysts

Fig. 1 shows the SEM images of the HAP-based catalysts. The bare HAP catalyst (Fig. 1(A)) consists of uniform nanoparticles with sizes between 10 nm to 20 nm. The particle sizes were determined by observing SEM images captured at multiple positions of the sample after loaded into SEM chamber. The nanoparticles tend to form irregular agglomerates. For HAP-CO<sub>3</sub> catalyst in Fig. 1(B), capsule-like particles are observed. Upon Pb substitution into HAP (Pb-HAP), the sample turned into rod-shaped clusters, as shown in Fig. 1(D). These rod-shaped clusters stacked on each other to form agglomerates. In the case of both cation and anion substituted HAP (Pb-HAP-CO<sub>3</sub>), a mixture of these morphologies were observed, as shown in Fig. 1(C). The cation and anion, or both cation and anion substitutions did not dramatically change the particle sizes of HAP catalysts. The surface areas of the HAP-based catalysts were determined from N<sub>2</sub> adsorption-desorption isotherms and the results are listed in Table 1. Consistent with SEM results, there is no significant change in surface areas across these four HAP-based catalysts.

XRD, FTIR and Raman spectra were used to study crystal polymorphs of the HAP-based catalysts, and the results are shown in Fig. 2(A)–(C). In Fig. 2(A), all peaks of the XRD spectrum for HAP, HAP-CO<sub>3</sub>, Pb-HAP and Pb-HAP-CO<sub>3</sub>, respectively, are consistent with the crystalline HAP phase. This result indicates that HAP crystalline structure was well-preserved after the incorporation of cation (Pb<sup>2+</sup>), anion (CO<sub>3</sub><sup>2-</sup>), or both cation and anion (Pb<sup>2+</sup> and CO<sub>3</sub><sup>2-</sup>), respectively. A further examination on the XRD spectra shows that the peak position and width are slightly different across the HAP-based catalysts. Firstly, the diffraction peaks of Pb-HAP and Pb-HAP-CO<sub>3</sub> are shifted to lower diffraction angles compared to HAP and HAP-CO<sub>3</sub> samples. The left-shift of the diffraction peaks was caused by Pb<sup>2+</sup> substitution, which has larger size than Ca<sup>2+</sup> ions. It is reported that the incorporation of larger cations in the apatite materials expands the lattice parameters of the hexagonal structure and thus leads to an increase in unit cell volume, which in turns causes a downward shifting in 2 $\theta$  diffraction angles [16]. Secondly, the diffraction peaks broaden from HAP to HAP-CO<sub>3</sub> and further to Pb-HAP-CO<sub>3</sub> and Pb-HAP, suggesting that the crystallinity of HAP-based catalysts decreased with incorporation of cation, anion, or both type of ions into the crystalline HAP material. The broadening and left-shifting of the diffraction peaks in Pb-HAP and Pb-HAP-CO<sub>3</sub> samples might also be resulted from the presence of trivial amount of other crystalline phases such as hydroxypyromorphite (HPY). It is reported that HPY can be precipitated from the synthesis mixture similar to that of HAP used in the present study [27,28]. The concurrent precipitation of HPY should be insignificant since no obvious diffraction peaks of HPY are observed in Fig. 2(A).



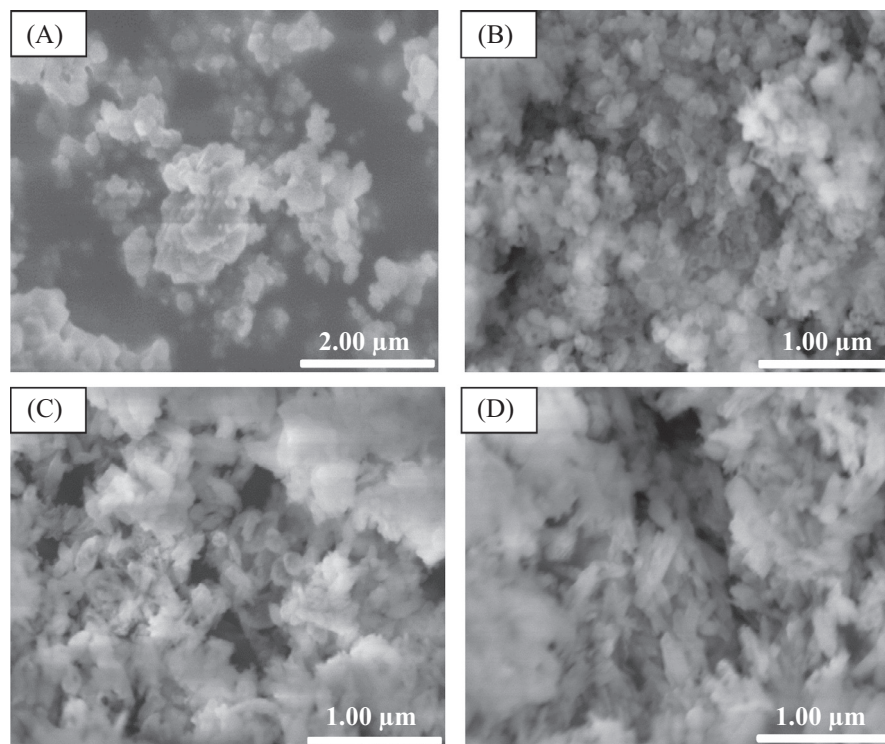


Fig. 1. SEM images showing morphologies of HAP-based catalysts: (A) HAP, (B) HAP-CO<sub>3</sub>, (C) Pb-HAP-CO<sub>3</sub>, and (D) Pb-HAP, respectively.

**Table 1**  
Chemical compositions and surface areas of HAP-based catalysts for OCM reactions.

Catalyst	Composition <sup>a</sup>			Composition <sup>b</sup>			Surface area <sup>c</sup> (m <sup>2</sup> /g)
	Pb/Ca	C/P	(Ca + Pb)/(P + C)	Pb/Ca	C/P	(Ca + Pb)/(P + C)	
HAP-CO <sub>3</sub>	0.00	0.48	1.64	0.00	0.29	1.56	36
HAP	0.00	0.00	1.65	0.00	0.00	1.59	39
Pb-HAP-CO <sub>3</sub>	0.17	0.44	1.73	0.33	0.34	1.64	37
Pb-HAP	0.16	0.00	1.60	0.47	0.00	1.63	49

<sup>a</sup> Determined by elemental analysis (ICP-OES).

<sup>b</sup> Determined from XPS measurement.

<sup>c</sup> Determined by BET method.

Fig. 2(B) illustrates the FTIR spectra of HAP-based catalysts. The spectrum of bare HAP shows all absorption bands characteristic for HAP [29]. For PO<sub>4</sub><sup>3-</sup> group, the  $\nu_1$  vibration (symmetric stretching) occurred at 942 cm<sup>-1</sup>, the  $\nu_3$  vibration (asymmetric stretching) centered at 1000 cm<sup>-1</sup> and 1100 cm<sup>-1</sup>, while  $\nu_1$  vibration (asymmetric bending) located at 563 cm<sup>-1</sup>, 600 cm<sup>-1</sup>, 942 cm<sup>-1</sup>, are all observed. The librational mode of OH<sup>-</sup> groups appears at 631 cm<sup>-1</sup>, suggesting the presence of hydroxyl groups in the bare HAP sample. Absence of any distinct bands in the range of 1400–1550 cm<sup>-1</sup> indicates that bare HAP does not contain detectable carbonate (CO<sub>3</sub><sup>2-</sup>) groups. The vibrational modes of PO<sub>4</sub><sup>3-</sup> groups are also observed in HAP-CO<sub>3</sub>, Pb-HAP-CO<sub>3</sub>, and Pb-HAP samples (Fig. 2(B)). This result suggests that the HAP structure was preserved upon cation, anion, or both substitutions, in agreement with the XRD results. The presence of broad vibrational bands centered at 1450 cm<sup>-1</sup> ( $\nu_3$  symmetric stretching of CO<sub>3</sub><sup>2-</sup>), characteristic for substitution of PO<sub>4</sub><sup>3-</sup> by CO<sub>3</sub><sup>2-</sup> (B-type) [30,31], in both HAP-CO<sub>3</sub> and Pb-HAP-CO<sub>3</sub> samples indicates the incorporation of CO<sub>3</sub><sup>2-</sup> into the HAP structure. The absorption band at 631 cm<sup>-1</sup> disappears in HAP-CO<sub>3</sub> and Pb-HAP-CO<sub>3</sub>, which resulted from the substitution of OH<sup>-</sup> by CO<sub>3</sub><sup>2-</sup> groups to form A-type substituted HAP. The FTIR spectra of HAP-CO<sub>3</sub> and Pb-HAP-CO<sub>3</sub> overall

suggest that AB-type CO<sub>3</sub><sup>2-</sup> substituted HAP was formed. The band at 872 cm<sup>-1</sup> in the FTIR spectra of these two samples result from both CO<sub>3</sub><sup>2-</sup> ( $\nu_2$  in-plane bending of CO<sub>3</sub><sup>2-</sup>) and HPO<sub>4</sub><sup>2-</sup> groups. It is reported that HPO<sub>4</sub><sup>2-</sup> groups are created to counterbalance the ionic charge when the OH<sup>-</sup> groups are replaced by CO<sub>3</sub><sup>2-</sup> in HAP, which overlaps with the CO<sub>3</sub><sup>2-</sup> band at 872 cm<sup>-1</sup>. The absence of CO<sub>3</sub><sup>2-</sup> bands and appearance of OH<sup>-</sup> band at 631 cm<sup>-1</sup> in Pb-HAP catalyst suggests no detectable CO<sub>3</sub><sup>2-</sup> groups in this sample. A slight shift of the vibration modes at 563 cm<sup>-1</sup> and 600 cm<sup>-1</sup> of PO<sub>4</sub><sup>3-</sup> groups toward lower wavenumbers in Pb-HAP and Pb-HAP-CO<sub>3</sub> reveals the presence of Pb<sup>2+</sup> ions [32], consistent with left-shift of 2 $\theta$  angles observed from XRD spectra. The features of FTIR spectra overall indicate that successful synthesis of cation (Pb<sup>2+</sup>), anion (CO<sub>3</sub><sup>2-</sup>, AB-type), and cation and anion (Pb<sup>2+</sup> and CO<sub>3</sub><sup>2-</sup>) substituted HAP catalysts.

Raman spectra in Fig. 2(C) are further used to understand the structural properties of the HAP-based catalysts. The vibration modes of PO<sub>4</sub><sup>3-</sup> groups in HAP structure,  $\nu_1$  (~960 to 961 cm<sup>-1</sup>),  $\nu_2$  (~430 to 450 cm<sup>-1</sup>),  $\nu_3$  (~1035 to 1048 cm<sup>-1</sup> and ~1070 to 1075 cm<sup>-1</sup>),  $\nu_4$  (~587 to 604 cm<sup>-1</sup>), confirm the apatite structure of all the catalysts [33]. The vibrational modes of the CO<sub>3</sub><sup>2-</sup> group are detected at 1073 cm<sup>-1</sup> in HAP-CO<sub>3</sub> and Pb-HAP-CO<sub>3</sub> ( $\nu_1$  mode

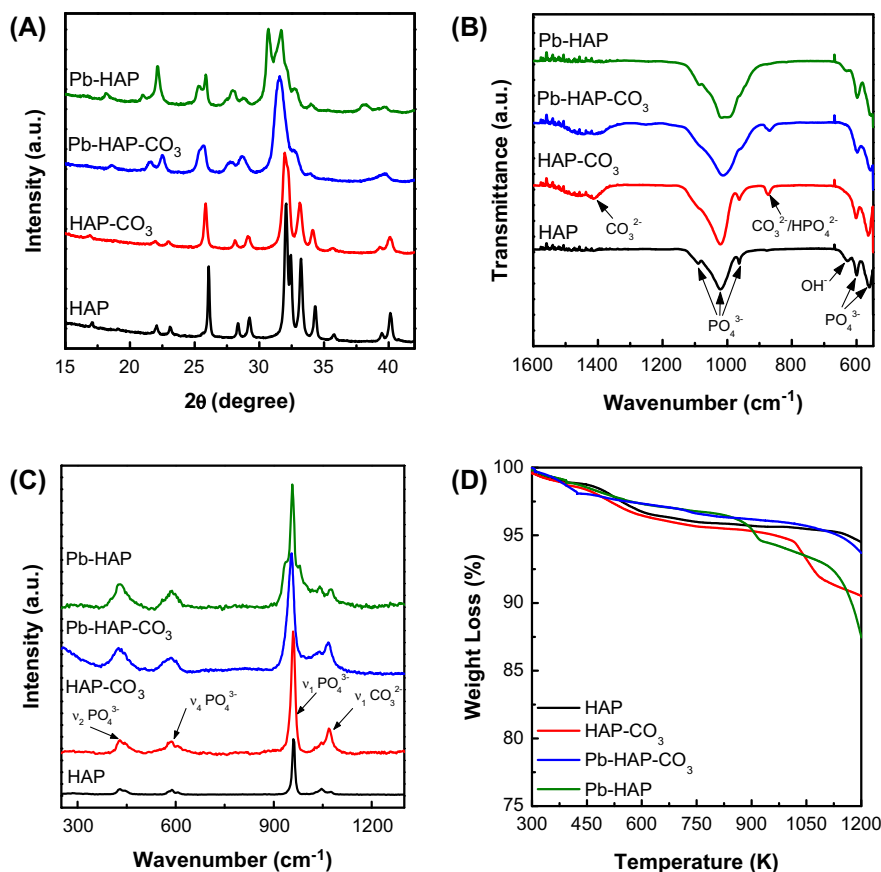


Fig. 2. XRD patterns (A), FT-IR spectra (B), Raman spectra (C), and TGA curves (D) of HAP-based catalysts, respectively, used for OCM reactions.

of B-type carbonate) [33], suggesting the presence of CO<sub>3</sub><sup>2-</sup> groups in these two samples, consistent with FTIR results above. The Raman peak at 960 cm<sup>-1</sup> undergoes a shift to lower wavenumber (928 cm<sup>-1</sup>) when the bare HAP was substituted with Pb<sup>2+</sup> ions, which is attributed to the stronger Pb–O interactions compared with the Ca–O ones in HAP catalysts [24]. The absence of vibrational band at ~700 cm<sup>-1</sup> in Fig. 2(C), which is assigned to an asymmetric P=O stretching mode of PO<sub>4</sub><sup>3-</sup> groups in the stoichiometric HAP, indicates that all the as-synthesized HAP-based catalysts are non-stoichiometric [21,34].

The thermal stability of the pre-calcined HAP-based catalysts was examined by TGA data presented in Fig. 2(D). The TGA measurement was conducted on the as-synthesized HAP samples after the drying step in vacuum oven. The slight decrease in weight for all the samples at temperature from 300 to 750 K is assigned to the evaporation of water bound to the catalyst surface or decomposition of adsorbed ammonium or nitrate ions used in the catalyst synthesis. The weight loss at the temperature above 1100 K was caused by the structure decomposition such as dehydroxylation since the temperature approaches the thermal stability limit of the HAP material [35]. In the temperature range of 750–1100 K, these four HAP-based catalysts showed different thermal decomposition behaviors. The bare HAP is stable, but HAP-CO<sub>3</sub> has two weight losses. The first weight loss at 1030 K was due to the removal of CO<sub>3</sub><sup>2-</sup> groups from A-type substitution, while the second loss at 1100 K was resulted from the decomposition of B-type substituted CO<sub>3</sub><sup>2-</sup> groups [36]. Pb-HAP also has two weight losses in this temperature range. The first one at 830 K is assigned to the loss of chlorine component used in the catalyst preparation [21]. The second one at 1030 K can be attributed to the decomposition of HAP into a Pb-containing β-tricalcium phosphate. Compared to

Pb-HAP and HAP-CO<sub>3</sub>, Pb-HAP-CO<sub>3</sub> has much better thermal stability in the temperature range of 750–1100 K.

### 3.2. Composition analysis of HAP-based catalysts

The bulk and surface stoichiometry of the HAP-based catalysts were determined using ICP-OES and XPS analyses, respectively, and the results are listed in Table 1. The Pb/Ca molar ratios in the synthesized samples are lower than the theoretical ratios (Pb/Ca = 0.25) used in catalyst synthesis. The cation/anion (i.e., (Ca + Pb)/(P + C)) molar ratios are slightly different, but close to the stoichiometric ratio of 1.67. The substitution of Pb<sup>2+</sup> cation or CO<sub>3</sub><sup>2-</sup> anion or both into the apatite structure did not alter the stoichiometry of HAP significantly. The surface element composition of the HAP-based catalysts in Table 1 shows that Pb/Ca ratios and (Ca + Pb)/(P + C) ratios are higher and lower, respectively, than those determined from ICP-OES analysis for these four catalyst samples. This result suggests that Pb content is rich on the surface of the Pb-HAP and Pb-HAP-CO<sub>3</sub> samples.

The basicity/acidity of the HAP catalyst and thus their catalytic performance in OCM reactions are known to depend strongly on the chemical state of the cationic sites. XPS data was therefore measured to identify the chemical states of the cationic species (Pb and Ca) in these post-calcined HAP-based catalysts. The presence of the desired elements (Ca, Pb, P and O) in the final product (Fig. 3(A)) indicates the successful preparation of the HAP-based catalysts. The binding energies of Pb 4f<sub>7/2</sub> and Pb 4f<sub>5/2</sub> of Pb-HAP are lower than those of Pb-HAP-CO<sub>3</sub> (Fig. 3(B)), which suggests Pb<sup>2+</sup> cations of Pb-HAP were positioned in a more electronegative environment than those of Pb-HAP-CO<sub>3</sub>. There are two types of Ca sites in HAP materials: 9-coordinated Ca<sub>11</sub> and 7-coordinated

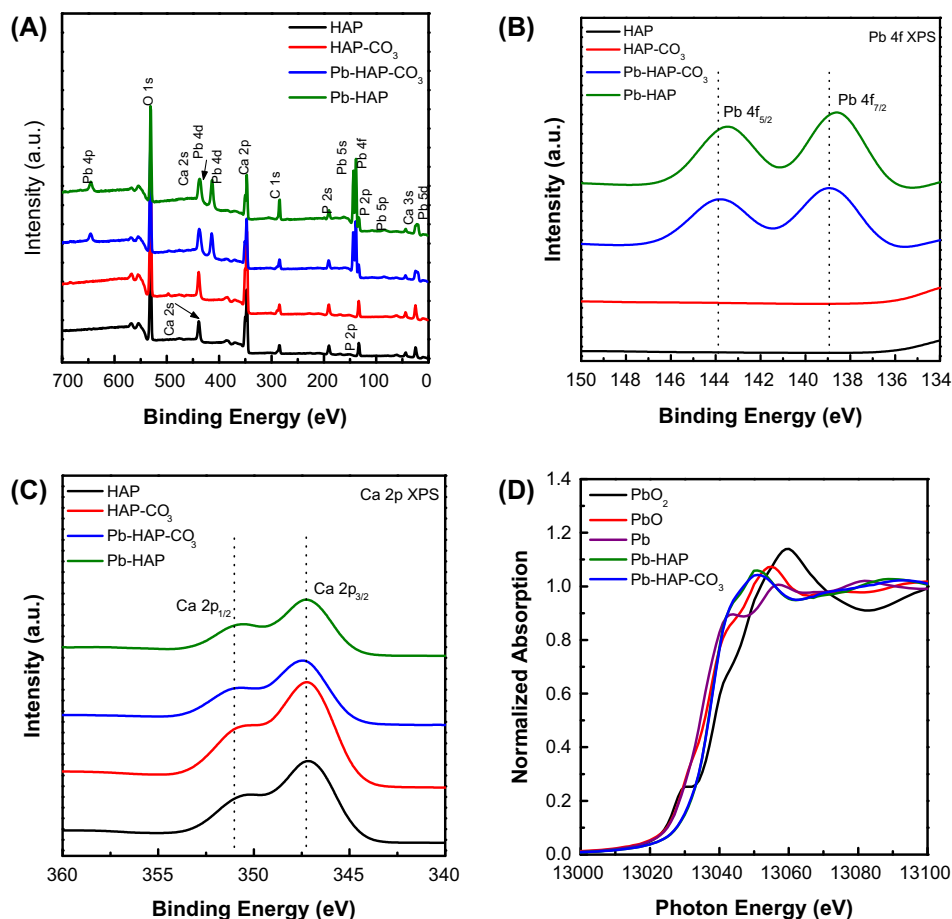


Fig. 3. XPS spectra (A), Pb 4f spectra (B), Ca 2p (C) and XANES spectra (D) of HAP-based catalysts, respectively, used for OCM reactions.

Ca<sub>[2]</sub>. The basicity of an atom is well known to increase with increase in its coordination number [37,38]. It is expected that Pb<sup>2+</sup> ions substitution for Ca<sub>[1]</sub> would possess more basicity compared to Ca<sub>[2]</sub>, and thus, Pb-HAP had more Pb<sup>2+</sup> ions positioned at the Ca<sub>[1]</sub> sites and higher basicity than Pb-HAP-CO<sub>3</sub> catalyst. The binding energies of Ca 2p<sub>3/2</sub> and Ca 2p<sub>1/2</sub> in the HAP-based catalysts, however, are almost identical (Fig. 3(C)). The XPS data suggests that the surface basicity of the catalyst is mainly related to the Pb<sup>2+</sup> ions and their chemical states. The oxidation state and possible phases of Pb ions in Pb-HAP and Pb-HAP-CO<sub>3</sub> were studied using Pb L<sub>3</sub> XANES spectra of Pb-HAP and Pb-HAP-CO<sub>3</sub>. Fig. 3(D) shows that both Pb-HAP and Pb-HAP-CO<sub>3</sub> exhibited similar adsorption energies at 13039 eV. The ~3 eV shift to higher energy than the metallic Pb foil indicates that Pb-HAP is in higher oxidation state than zero. Pb L<sub>3</sub> edge represents mainly the 2p → 6p transition for Pb<sup>2+</sup>-containing structures. On the other hand, a pre-edge at ~13027 eV representing 2p → 6s transition can be observed for Pb<sup>4+</sup> ions (e.g., PbO<sub>2</sub>). The absence of pre-edge features in Pb-HAP and Pb-HAP-CO<sub>3</sub> XANES spectra indicates that most Pb ions in the catalysts are in the Pb<sup>2+</sup> state. There is no overlapping between Pb-HAP and PbO reference, indicating that Pb<sup>2+</sup> ions exist in the phase other than PbO.

### 3.3. Surface acidity of HAP-based catalysts

The surface acidity and acid strength of the HAP-based catalysts were investigated using NH<sub>3</sub>-TPD. Phosphate groups in bare HAP are responsible for the acidity of the catalyst, whereas the Ca<sup>2+</sup> ions are responsible for the basicity [36]. An increase in the basicity and

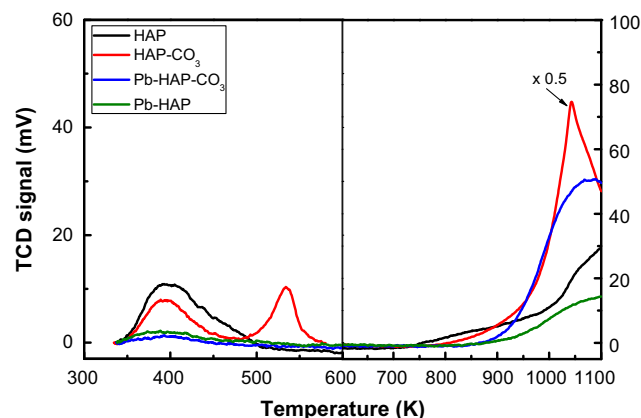


Fig. 4. NH<sub>3</sub>-TPD profiles of HAP, HAP-CO<sub>3</sub>, Pb-HAP and Pb-HAP-CO<sub>3</sub> catalysts.

acidity is expected upon Pb<sup>2+</sup> and CO<sub>3</sub><sup>2-</sup> substitution into the HAP structure, respectively. Fig. 4 shows NH<sub>3</sub>-desorption peaks exist in the regions of lower temperatures (<600 K), medium temperatures (750–930 K), and also at higher temperatures (>930 K), respectively. This indicates the presence of weak, medium and strong acid sites in the HAP-based catalyst samples. The broad variation in peak intensity across these four HAP-based catalyst samples reveals that the catalysts differ from each other widely in their total number of acid sites and also in the strength of the acid sites. In the low temperature region in Fig. 4, bare HAP exhibits a broad peak centered at 440 K. This desorption peak is split

into two peaks, one shifted downwards to 400 K and the other shifted upwards to 520 K in the sample of HAP-CO<sub>3</sub>. When Pb<sup>2+</sup> ions were incorporated into the HAP-CO<sub>3</sub> to form Pb-HAP-CO<sub>3</sub>, the acidity of the catalyst is significantly decreased, as reflected by the reduced intensity of the NH<sub>3</sub>-TPD peaks below 600 K. Pb-HAP shows similar NH<sub>3</sub>-desorption peak to that of Pb-HAP-CO<sub>3</sub>. The weak acidity in the catalysts follows the order of HAP-CO<sub>3</sub> > HAP > Pb-HAP ~ Pb-HAP-CO<sub>3</sub>. The medium acidity in these four catalysts shows the same trend to that of weak acidity. In the high temperature range (750–930 K), HAP-CO<sub>3</sub> and HAP have higher peak intensity than that of Pb-HAP and Pb-HAP-CO<sub>3</sub>. The order of NH<sub>3</sub>-TPD peak intensity is HAP-CO<sub>3</sub> > Pb-HAP-CO<sub>3</sub> > HAP > Pb-HAP.

The liberation of NH<sub>3</sub> in the low temperature range in Fig. 4 is mainly attributed to the PO<sub>4</sub><sup>3-</sup> groups present in the HAP catalysts [39]. The medium and high temperature NH<sub>3</sub>-desorption peaks are caused by the co-existed PO<sub>4</sub><sup>3-</sup>, CO<sub>3</sub><sup>2-</sup> and HPO<sub>4</sub><sup>2-</sup> groups. The AB-type CO<sub>3</sub><sup>2-</sup> substituted HAP, as suggested by FTIR data, contains both CO<sub>3</sub><sup>2-</sup> groups in the A and B sites and HPO<sub>4</sub><sup>2-</sup> that is resulted from substitution of OH<sup>-</sup> groups by CO<sub>3</sub><sup>2-</sup> [39]. The broad and strong high temperature desorption peak in HAP-CO<sub>3</sub> and Pb-HAP-CO<sub>3</sub> might also be caused by the release of CO<sub>2</sub> from CO<sub>3</sub><sup>2-</sup> groups in the apatite structure [40]. It is generally accepted that the strength and quantity of the acid sites are directly related to desorption temperature and intensity in NH<sub>3</sub>-TPD analysis. Therefore, the NH<sub>3</sub>-TPD data confirms that the acidity HAP-based catalysts was tuned upon Pb<sup>2+</sup>, CO<sub>3</sub><sup>2-</sup>, or both substitutions. The absence of CO<sub>3</sub><sup>2-</sup> from Pb-HAP-CO<sub>3</sub> catalyst further reduced the acidity of the catalyst since Pb-HAP only showed very weak NH<sub>3</sub> desorption peaks. The reduction and enhancement in acidity upon Pb<sup>2+</sup> and CO<sub>3</sub><sup>2-</sup> substitution, respectively, are consistent with composition and XPS analyses discussed above.

### 3.4. Performance of HAP-based catalysts in OCM reactions

The activity, stability and selectivity of the HAP-based catalysts in OCM reactions were firstly examined at 973 K and 101 kPa pressure. Fig. 5(A) shows that the methane conversion followed a sequence of Pb-HAP-CO<sub>3</sub> > HAP > Pb-HAP > HAP-CO<sub>3</sub>. In addition, HAP and Pb-HAP-CO<sub>3</sub> were more stable than Pb-HAP and HAP-CO<sub>3</sub>. The slight decrease in activity of Pb-HAP with time on steam (TOS) and abrupt drop in activity of HAP-CO<sub>3</sub> in the beginning of the reaction was resulted from their structural instability, as shown by the TGA data in Fig. 2(D). It should be noted that Pb-HAP-CO<sub>3</sub> maintained its activity and stability in the OCM reaction conditions. Fig. 5(B) shows the product selectivity of the

HAP-based catalysts with TOS of 6 h and methane conversion of 23%. The C<sub>2</sub> selectivity monotonically increases from HAP-CO<sub>3</sub>, HAP, Pb-HAP-CO<sub>3</sub> to Pb-HAP catalysts. The activity and selectivity of these four HAP-based catalysts follows the reverse order of low and medium temperature desorption peak intensity in NH<sub>3</sub>-TPD profiles. Pb-HAP and Pb-HAP-CO<sub>3</sub> are more active and selective in C<sub>2</sub> formation. It is reported that Pb<sup>2+</sup> ions form covalent bonds with carbon, which can stabilize methyl radicals and enable pairwise reaction of methyl radicals to form C<sub>2</sub> products [17,24,41–43]. In HAP and HAP-CO<sub>3</sub> catalysts, the acidic environment promotes dissociative adsorption and builds up a strong interaction between the catalyst surfaces and C<sub>2</sub> products. C<sub>2</sub> products tend to stay on the surface of the catalyst which then undergoes secondary oxidation process to form CO and CO<sub>2</sub> [44]. The trend of C<sub>2</sub> selectivity across these catalysts is consistent with their surface composition and acidity changes. This result suggests that the tunable composition of the HAP-based catalysts by ion substitutions influences their physicochemical properties and consequently the selectivity in OCM reactions.

Methane conversion and product selectivity in OCM reactions over the HAP-based catalysts at different temperatures were studied. As shown in Fig. 6(A), the methane conversion over Pb-HAP and Pb-HAP-CO<sub>3</sub> increased significantly with increasing temperature, while the conversion increased only slightly over HAP-CO<sub>3</sub> and HAP catalysts. This suggests that Pb species is the active component in the HAP-based catalyst for methane activation in OCM reactions, consistent with previous report [16]. Fig. 6(B)–(D) shows the selectivity to C<sub>2</sub>, CO<sub>2</sub>, and CO products across these four catalysts at different reaction temperatures. C<sub>2</sub> production was favored with increasing temperature, CO<sub>2</sub> formation was inhibited, while CO formation was kept almost constant. It should be noted that HAP-CO<sub>3</sub> generated more CO than other HAP-based catalysts (Figs. 5(B) and 6(D)). The methane reforming or reverse water gas shift reactions, caused by the acidity of HAP-CO<sub>3</sub> catalyst, can potentially contribute to the CO product.

The effects of methane to oxygen ratio in OCM reactions was studied on the selected Pb-HAP and Pb-HAP-CO<sub>3</sub> catalysts at different temperatures. Fig. 7 shows the methane to oxygen ratio is tuned by varying oxygen partial pressure (8.1/11.3/21.0/32.0/40.7 kPa, respectively) while keeping a constant methane partial pressure of 25 kPa, and helium was used as the balance gas. CH<sub>4</sub> conversion decreased with increasing CH<sub>4</sub>/O<sub>2</sub> ratio while C<sub>2</sub> selectivity increased with increasing CH<sub>4</sub>/O<sub>2</sub> ratio at all the studied temperatures for both catalysts. Higher CH<sub>4</sub>/O<sub>2</sub> ratio indicates lower O<sub>2</sub> concentration in the gas phase in the reaction, which in turns promotes C<sub>2</sub> formation since most of the O<sub>2</sub> are activated

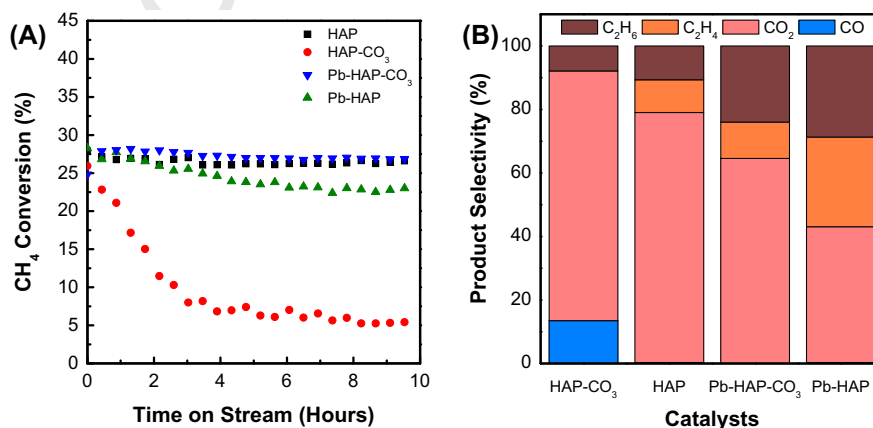


**Fig. 5.** (A) Methane conversion with time-on-stream in OCM reactions and (B) product selectivity for OCM reactions over HAP-based catalysts at 23% conversion under 973 K and 101 kPa pressure conditions and a space velocity of 8800 mL g<sub>cat</sub><sup>-1</sup> h<sup>-1</sup>.



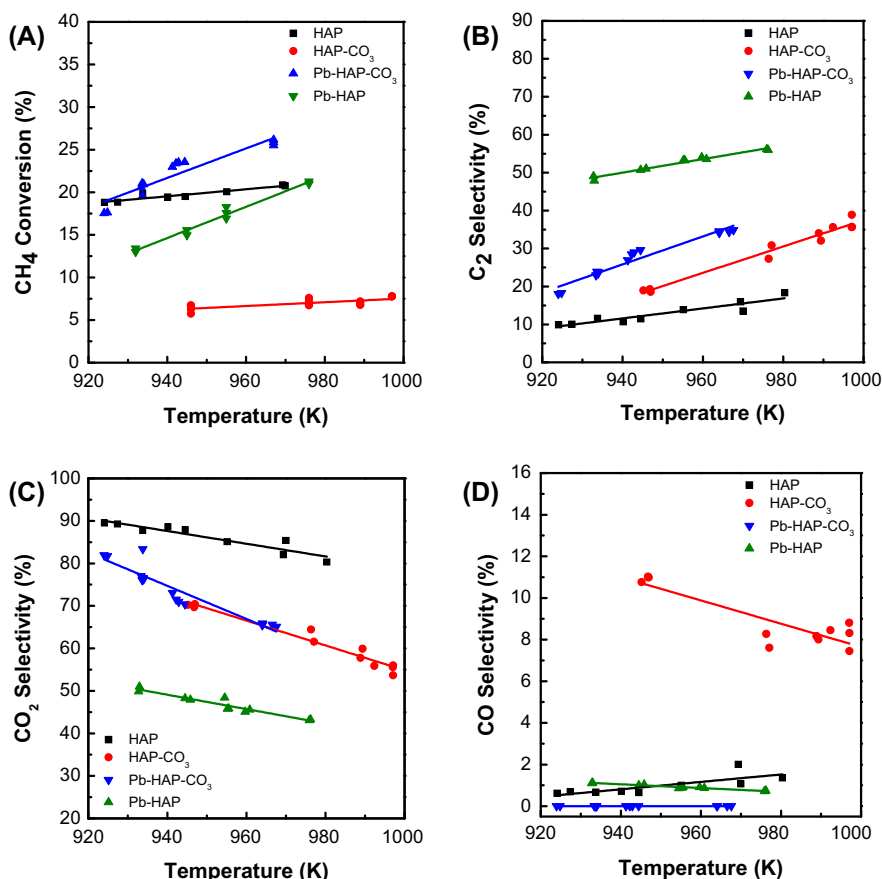


**Fig. 6.** Methane conversion (A) and product selectivity (C<sub>2</sub> (B); CO<sub>2</sub> (C); CO (D)) of OCM reactions over HAP-based catalysts at different temperatures ( $P_{\text{CH}_4} = 27.1$  kPa,  $P_{\text{O}_2} = 11.0$  kPa, total flow =  $46 \text{ ml min}^{-1}$ , He was used as the balance gas).

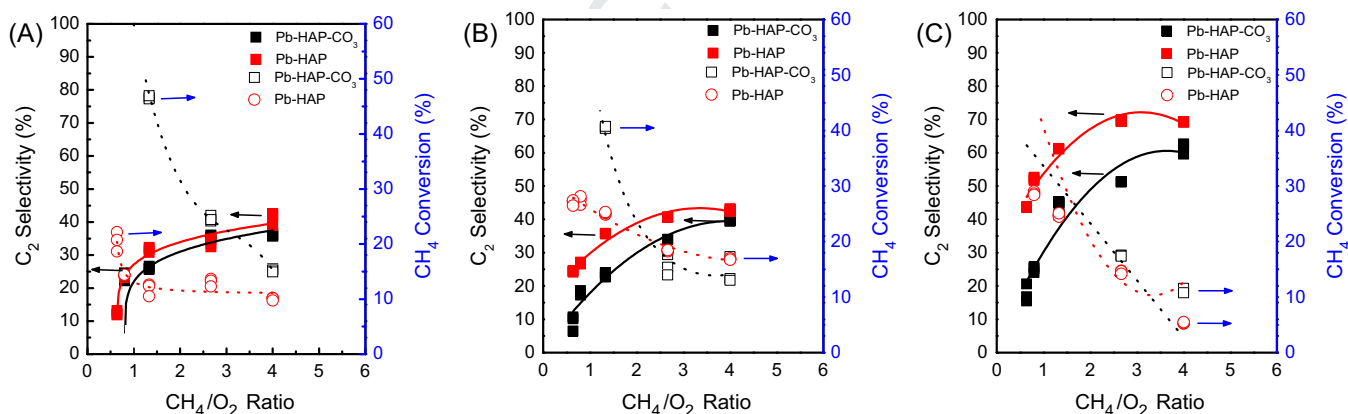


**Fig. 7.** Effect of methane-to-oxygen ( $\text{CH}_4/\text{O}_2$ ) ratio on C<sub>2</sub> selectivity and CH<sub>4</sub> conversion at (A) 923 K, (B) 943 K and (C) 973 K at a constant CH<sub>4</sub> partial pressure of 25 kPa (Total flow rate =  $46 \text{ mL min}^{-1}$ ) (filled symbol represents C<sub>2</sub> selectivity, unfilled symbol represents CH<sub>4</sub> conversion).

on the surface of the catalyst. On the other hand, higher CH<sub>4</sub>/O<sub>2</sub> ratio, i.e., lower O<sub>2</sub> concentration, leads to lower CH<sub>4</sub> conversion. Fig. 7(A) also demonstrates that CH<sub>4</sub> conversion over Pb-HAP-CO<sub>3</sub> catalyst was higher than Pb-HAP catalysts when the reaction temperature was low (923 K). With an increase in reaction temperature to 943 K (Fig. 7(B)) or 973 K (Fig. 7(C)), Pb-HAP and Pb-HAP-CO<sub>3</sub> showed similar methane conversion. The selectivity to C<sub>2</sub> product, however, showed opposite trend with the reaction temperature. At the temperature of 923 K (Fig. 7(A)), both catalysts have similar C<sub>2</sub> selectivity in OCM reactions. With increasing reaction temperature to 943 K (Fig. 7(B)), Pb-HAP has higher C<sub>2</sub>

selectivity than that of Pb-HAP-CO<sub>3</sub>. The differences in C<sub>2</sub> selectivity is more evident when the temperature was further increased to 973 K (Fig. 7(C)). With the available C<sub>2</sub> selectivity and CH<sub>4</sub> conversion data, the C<sub>2</sub> yield, which is product of C<sub>2</sub> selectivity and CH<sub>4</sub> conversion, can be accessed. At lower reaction temperature (923 K), Pb-HAP-CO<sub>3</sub> showed higher C<sub>2</sub> yield than that of Pb-HAP catalyst. When the reaction temperature was increased to 973 K, the C<sub>2</sub> yield was higher in Pb-HAP than Pb-HAP-CO<sub>3</sub>. These results suggest that the C<sub>2</sub> production over Pb-HAP-CO<sub>3</sub> can be optimized under certain reaction conditions. Overall, the OCM reaction data indicate that the catalytic performance of the HAP-based catalysts



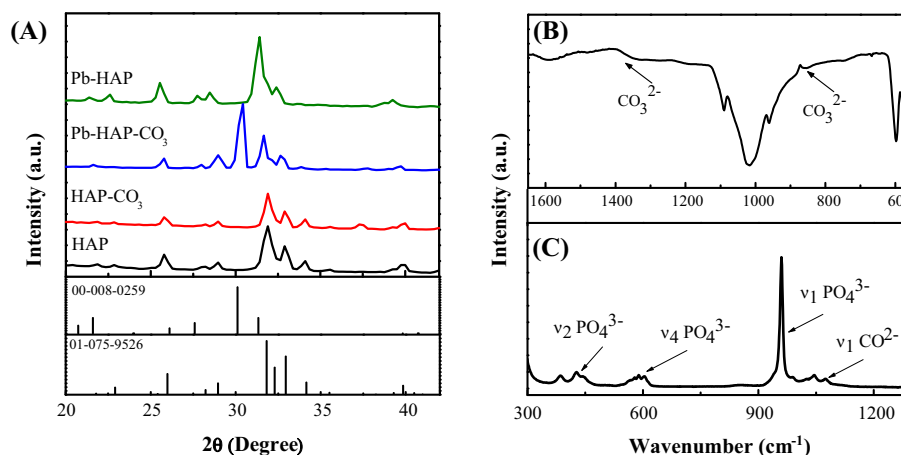


**Fig. 8.** XRD pattern (A), FTIR (B) and (C) Raman of Pb-HAP-CO<sub>3</sub> after 10-h of OCM reaction. For comparison purpose, XRD patterns of HAP, HAP-CO<sub>3</sub> and Pb-HAP samples after 10 h OCM reaction have also been presented in (A).

can be tuned upon cation or anion substitutions in the apatite structure. Given the catalyst stability, activity, selectivity and O<sub>2</sub> permeable properties under optimized reaction condition, Pb-HAP-CO<sub>3</sub> can be a potential catalyst to be integrated in membrane reactor to enable effective OCM reactions with side feeding of O<sub>2</sub> through the membrane.

The crystallinity and structure of Pb-HAP-CO<sub>3</sub> were studied after OCM reactions. Fig. 8 shows the XRD, FTIR and Raman data, respectively, collected on Pb-HAP-CO<sub>3</sub> sample after TOS of 10 h. For comparison purpose, the XRD patterns of three other catalyst samples (HAP, Pb-HAP and Pb-HAP-CO<sub>3</sub>) were measured and included in Fig. 8(A). In comparison with Fig. 2(A), the sharpness of the XRD peaks in all the samples was decreased, which indicates that crystallinity of the HAP-based catalyst might be reduced after OCM reaction. The HAP, Pb-HAP and HAP-CO<sub>3</sub> still maintain their initial diffraction peak positions. The Pb-HAP-CO<sub>3</sub>, however, formed a new diffraction peak centered at 2θ ~ 30°. This diffraction peak can be indexed to the HPY structure. HPY has been reported to be synthesized from mixture of lead and phosphate precursor solutions [27,28]. In the OCM reaction condition, acidic environment of Pb-HAP-CO<sub>3</sub> may facilitate the transformation of the HAP to HPY structure. It should be noted that the catalytic performance of Pb-HAP-CO<sub>3</sub> did not decrease with time on stream of the OCM reaction (Fig. 5). The FTIR (Fig. 8(B)) spectra of Pb-HAP-CO<sub>3</sub> sample after OCM reaction shows that the vibrational bands centered at 1450 cm<sup>-1</sup>, which corresponds to ν<sub>3</sub> symmetric stretching of CO<sub>3</sub><sup>2-</sup>. The band at 872 cm<sup>-1</sup>, which results from CO<sub>3</sub><sup>2-</sup> (ν<sub>2</sub> in-plane bending of CO<sub>3</sub><sup>2-</sup>) group, can still be observed after 10 h of reaction, implying that CO<sub>3</sub><sup>2-</sup> group was still present in the HAP structure. In the case of Raman spectra (Fig. 8(C)) of Pb-HAP-CO<sub>3</sub>, the vibrational modes of the CO<sub>3</sub><sup>2-</sup> group are detected at 1073 cm<sup>-1</sup> after 10 h of OCM reaction, again indicating that Pb-HAP-CO<sub>3</sub> still maintained the carbonate group inside the structure.

#### 4. Conclusions

The HAP apatite structure with cation (Pb<sup>2+</sup>), anion (CO<sub>3</sub><sup>2-</sup>), or both (Pb<sup>2+</sup> and CO<sub>3</sub><sup>2-</sup>) substitutions have been synthesized. The physicochemical properties and catalytic behaviors of the HAP-based catalysts were assessed by a variety of characterizations and OCM catalysis tests. The Pb<sup>2+</sup> and CO<sub>3</sub><sup>2-</sup> substitutions changed the composition and physicochemical properties of the HAP catalyst. The Pb-HAP-CO<sub>3</sub> with both Pb<sup>2+</sup> and CO<sub>3</sub><sup>2-</sup> substitutions exhibited the best thermal structural stability. The tunable composition of the HAP-based catalysts, and thus the tunable surface acidity

environment, influences the catalytic behaviors of the catalysts in OCM reactions. The OCM catalysis studies showed that C<sub>2</sub> selectivity increased with Pb<sup>2+</sup> substitution in the catalysts whereas Pb-HAP-CO<sub>3</sub> exhibited better stability in comparison with Pb-HAP. At the examined reaction temperatures of 923, 943, and 973 K, the CH<sub>4</sub> conversion and C<sub>2</sub> selectivity decreased and increased, respectively, with increasing CH<sub>4</sub>/O<sub>2</sub> ratios. The C<sub>2</sub> yield showed a strong dependence on the composition of HAP-based catalysts and reaction conditions. The present work is for the first time a systematic examination of the effects of composition of HAP-based apatite materials on OCM reactions. The synthesis method, understating of the correlations between the composition, property, and catalytic performance of HAP-based catalysts are applicable to a range of apatite structured ceramic materials, which are potential membrane materials for OCM reaction in membrane reactors.

#### Acknowledgements

The authors gratefully acknowledge financial support from the American Chemical Society Petroleum Research Fund (ACS-PRF) and National Science Foundation (NSF-CBET 1264599). We acknowledge the support of Maryland NanoCenter and its NispLab. The NispLab is supported in part by the NSF as a MRSEC Shared Experimental Facility. MRCAT operations are supported by the Department of Energy and the MRCAT member institutions. This research used resources of the Advanced Photon Source, a U.S. Department of Energy (DOE) Office of Science User Facility operated for the DOE Office of Science by Argonne National Laboratory under Contract No. DE-AC02-06CH11357.

#### References

- [1] Holmen A. Direct conversion of methane to fuels and chemicals. *Catal Today* 2009;142:2–8.
- [2] Lunsford JH. Catalytic conversion of methane to more useful chemicals and fuels: a challenge for the 21st century. *Catal Today* 2000;63:165–74.
- [3] Iglesia E. Design, synthesis, and use of cobalt-based Fischer–Tropsch synthesis catalysts. *Appl Catal A-Gen* 1997;161:59–78.
- [4] Guo X, Fang G, Li G, Ma H, Fan H, Yu L, et al. Direct, nonoxidative conversion of methane to ethylene, aromatics, and hydrogen. *Science* 2014;344:616–9.
- [5] Zhang J-Z, Long MA, Howe RF. Molybdenum ZSM-5 zeolite catalysts for the conversion of methane to benzene. *Catal Today* 1998;44:293–300.
- [6] Keller GE, Bhasin MM. Synthesis of ethylene via oxidative coupling of methane: I. Determination of active catalysts. *J Catal* 1982;73:9–19.
- [7] Lunsford JH. The catalytic oxidative coupling of methane. *Angew Chem Int Ed* 1995;34:970–80.
- [8] Su YS, Ying JY, Green Jr WH. Upper bound on the yield for oxidative coupling of methane. *J Catal* 2003;218:321–33.

- [9] Othman NH, Wu Z, Li K. A micro-structured  $\text{La}_{0.6}\text{Sr}_{0.4}\text{Co}_{0.2}\text{Fe}_{0.8}\text{O}_{3-\delta}$  hollow fibre membrane reactor for oxidative coupling of methane. *J Membr Sci* 2014;468:31–41.
- [10] Coronas J, Menéndez M, Santamaria J. Methane oxidative coupling using porous ceramic membrane reactors—II. Reaction studies. *Chem Eng Sci* 1994;49:2015–25.
- [11] Akin FT, Lin YS. Oxidative coupling of methane in dense ceramic membrane reactor with high yields. *AIChE J* 2002;48:2298–306.
- [12] Suchanek W, Yoshimura M. Processing and properties of hydroxyapatite-based biomaterials for use as hard tissue replacement implants. *J Mater Res* 1998;13:94–117.
- [13] Yamashita K, Kitagaki K, Umegaki T. Thermal instability and proton conductivity of ceramic hydroxyapatite at high temperatures. *J Am Ceram Soc* 1995;78:1191–7.
- [14] Ellis DE, Terra J, Warschkow O, Jiang M, Gonzalez GB, Okasinski JS, et al. A theoretical and experimental study of lead substitution in calcium hydroxyapatite. *PCCP* 2006;8:967–76.
- [15] Marchat D, Zymelka M, Coelho C, Gremillard L, Joly-pottuz L, Babonneau F, et al. Accurate characterization of pure silicon-substituted hydroxyapatite powders synthesized by a new precipitation route. *Acta Biomater* 2013;9:6992–7004.
- [16] David S, Serena MB. Production of zinc substituted hydroxyapatite using various precipitation routes. *Biomater* 2013;34:25003.
- [17] Lee K-Y, Han Y-C, Suh DJ, Park T-J. Pb-substituted hydroxyapatite catalysts prepared by coprecipitation method for oxidative coupling of methane. *Stud Surf Sci Catal* 1998;119:385–90.
- [18] Tönsuaadu K, Gruselle M, Villain F, Thouvenot R, Peld M, Mikli V, et al. A new glance at ruthenium sorption mechanism on hydroxy, carbonate, and fluor apatites: analytical and structural studies. *J Colloid Interface Sci* 2006;304:283–91.
- [19] Meirer F, Pemmer B, Pepponi G, Zoeger N, Wobrauschek P, Sprio S, et al. Assessment of chemical species of lead accumulated in tidemarks of human articular cartilage by X-ray absorption near-edge structure analysis. *J Synchrotron Radiat* 2011;18:238–44.
- [20] Mostafa NY. Characterization, thermal stability and sintering of hydroxyapatite powders prepared by different routes. *Mater Chem Phys* 2005;94:333–41.
- [21] Park JH, Lee D-W, Im S-W, Lee YH, Suh D-J, Jun K-W, et al. Oxidative coupling of methane using non-stoichiometric lead hydroxyapatite catalyst mixtures. *Fuel* 2012;94:433–9.
- [22] Gruselle M. Apatites: a new family of catalysts in organic synthesis. *J Organomet Chem* 2015;793:93–101.
- [23] Bouhaouss A, Laghizil A, Bensaoud A, Ferhat M, Lorent G, Livage J. Mechanism of ionic conduction in oxy and hydroxyapatite structures. *Int J Inorg Mater* 2001;3:743–7.
- [24] Matsumura Y, Moffat J. Catalytic oxidative coupling of methane over hydroxyapatite modified with lead. *Catal Lett* 1993;17:197–204.
- [25] Tanaka Y, Kikuchi M, Tanaka K, Hashimoto K, Hojo J, Nakamura M, et al. Fast oxide ion conduction due to carbonate substitution in hydroxyapatite. *J Am Ceram Soc* 2010;93:3577–9.
- [26] Wu Y, Emdadi L, Wang Z, Fan W, Liu D. Textural and catalytic properties of Mo loaded hierarchical meso-/microporous lamellar MFI and MWW zeolites for direct methane conversion. *Appl Catal A-Gen* 2014;470:344–54.
- [27] Lower SK, Maurice PA, Traina SJ, Carlson EH. Aqueous Pb sorption by hydroxylapatite: applications of atomic force microscopy to dissolution, nucleation, and growth studies. *Am Mineral* 1998;83:147–58.
- [28] Narasaraaju TSB, Singh RP, Rao VLN. A new method of preparation of solid solutions of calcium and lead hydroxylapatites. *J Inorg Nucl Chem* 1972;34:2072–4.
- [29] Hongquan Z, Yuhua Y, Youfa W, Shipu L. Morphology and formation mechanism of hydroxyapatite whiskers from moderately acid solution. *Mater Res* 2003;6:111–5.
- [30] Gibson IR, Bonfield W. Novel synthesis and characterization of an AB-type carbonate-substituted hydroxyapatite. *J Biomed Mater Res* 2002;59:697–708.
- [31] Genge MJ, Jones AP, Price GD. An infrared and Raman study of carbonate glasses: implications for the structure of carbonatite magmas. *Geochim Cosmochim Acta* 1995;59:927–37.
- [32] Hadrich A, Lautié A, Mhiri T. Vibrational study and fluorescence bands in the FT-Raman spectra of  $\text{Ca}_{10-x}\text{Pb}_x(\text{PO}_4)_6(\text{OH})_2$  compounds. *Spectrochim Acta A-Mol Biomol Spectrosc* 2001;57:1673–81.
- [33] Penel G, Delfosse C, Descamps M, Leroy G. Composition of bone and apatitic biomaterials as revealed by intravital Raman microspectroscopy. *Bone* 2005;36:893–901.
- [34] Smith R, Rehman I. Fourier transform Raman spectroscopic studies of human bone. *J Mater Sci Mater Med* 1994;5:775–8.
- [35] Liao C-J, Lin F-H, Chen K-S, Sun J-S. Thermal decomposition and reconstitution of hydroxyapatite in air atmosphere. *Biomaterials* 1999;20:1807–13.
- [36] Silvester L, Lamonier J-F, Vannier R-N, Lamonier C, Capron M, Mamede A-S, et al. Structural, textural and acid-base properties of carbonate-containing hydroxyapatites. *J Mater Chem A* 2014;2:11073–90.
- [37] Climent MJ, Corma A, Iborra S, Epping K, Veltz A. Increasing the basicity and catalytic activity of hydrotalcites by different synthesis procedures. *J Catal* 2004;225:316–26.
- [38] Yamaguchi K, Ebitani K, Yoshida T, Yoshida H, Kaneda K. Mg–Al mixed oxides as highly active acid–base catalysts for cycloaddition of carbon dioxide to epoxides. *J Am Chem Soc* 1999;121:4526–7.
- [39] Diallo-Garcia S, Osman MB, Krafft J-M, Casale S, Thomas C, Kubo J, et al. Identification of surface basic sites and acid-base pairs of hydroxyapatite. *J Phys Chem C* 2014;118:12744–57.
- [40] Yasukawa A, Kandori K, Ishikawa T. TPD-TG-MS study of carbonate calcium hydroxyapatite particles. *Calcif Tissue Int* 2003;72:243–50.
- [41] Matsumura Y, Sugiyama S, Hayashi H, Moffat JB. Lead-calcium hydroxyapatite: cation effects in the oxidative coupling of methane. *J Solid State Chem* 1995;114:138–45.
- [42] Matsumura Y, Moffat JB, Sugiyama S, Hayashi H, Shigemoto N, Saitoh K. Selective oxidative coupling of methane catalysed over hydroxyapatite ion-exchanged with lead. *J Chem Soc, Faraday Trans* 1994;90:2133–40.
- [43] Kong JI, Jung JS, Choi JG, Lee SH. Catalytic activity of  $\text{LiSBTe}_2$  for oxidative coupling of methane. *Appl Catal A-Gen* 2000;204:241–50.
- [44] Zaera F. Key unanswered questions about the mechanism of olefin hydrogenation catalysis by transition-metal surfaces: a surface-science perspective. *PCCP* 2013;15:11988–2003.